THESIS FOR THE DEGREE OF LICENTIATE OF ENGINEERING IN SOLID AND STRUCTURAL MECHANICS

RVE generation and computational homogenization of structural battery electrolytes

Vinh Tu

CHALMERS
UNIVERSITY OF TECHNOLOGY

Department of Industrial and Materials Science
Division of Material and Computational Mechanics
CHALMERS UNIVERSITY OF TECHNOLOGY
Gothenburg, Sweden, 2022

RVE generation and computational homogenization of structural battery electrolytes

Vinh Tu

Technical Report No. IMS-2022-5
This thesis has been prepared using LaTeX.
Department of Industrial and Materials Science
Chalmers University of Technology
SE-412 96 Gothenburg, Sweden
Phone: +46 (0)31 772 1000

Cover:
Illustration of a macroscale problem (left) based on precomputed upscaling of a 3D RVE (right). The red arrows represent the mass flux direction of Li-ions.
Printed by Chalmers Reproservice
Gothenburg, Sweden, April 2022

Department of Industrial and Materials Science
Division of Material and Computational Mechanics
Chalmers University of Technology

Abstract

The structural battery is multifunctional in the sense that it is able to carry mechanical loads, and at the same time store and deliver energy. This is made possible due to carbon fibers' ability to act not only as structural reinforcement materials, but also as electrode components. While conventional batteries rely solely on liquid electrolyte to allow for ion transfer between the electrodes, structural batteries exploit the so-called structural battery electrolyte (SBE). The SBE consists of two continuous phases; a porous polymer skeleton and a liquid electrolyte. The role of the liquid electrolyte is to allow for ion transfer, while the porous polymer skeleton contributes to the mechanical properties. In short, the structural battery consists of carbon fibers (acting as electrodes) embedded in an SBE.

In the first part of the thesis, we study the multifunctional performance of various SBE microstructures by performing virtual material testing on artificially generated Representative Volume Elements (RVEs). In particular, we obtain the effective ionic conductivity by solving a diffusion equation with Fick's law, and the effective stiffness by assuming linear elasticity. The generated RVEs and the predicted performance are compared to experimental data.

The second part covers the development of a multiscale modeling framework for electrochemically coupled ion transport in SBEs. After establishing the governing equations, we exploit Variationally Consistent Homogenization (VCH) to obtain a two-scale model. If the subscale RVE problem exhibits negligible transient effects for length scales relevant to the studied application, then an assumption of micro-stationarity can be introduced. This opens up for the possibility to devise a numerically efficient solution scheme for the macroscale problem that is based on a priori upscaling of the effective response. The procedure is demonstrated in a set of numerical examples, including validation toward a (single-scale) reference solution.

Keywords: Li-ion based structural batteries, structural battery electrolyte, RVE generation, electrochemical transport, computational homogenization.

to my beloved girlfriend, Monica

Preface

The work in this thesis was carried out from June 2019 to April 2022 at the Division of Material and Computational Mechanics, Department of Industrial and Materials Science, Chalmers University of Technology. The funding from Swedish Research Council (VR) under Grant 2017-05192 is gratefully acknowledged.

Acknowledgments

First of all, I would like to thank Professor Ralf Jänicke and Professor Fredrik Larsson for being excellent supervisors. Thank you for your patience, support and guidance. As your PhD student, I truly feel grateful for all that you have done for me! Many thanks to Professor Kenneth Runesson for co-supervising me and always sharing his insightful inputs. Thanks to Professor Leif E. Asp for always being interested in my work and initiating fruitful collaborations. It really has been great so far, and I look forward to continue working with all of you for the remaining part of my project!

I would also like to thank my colleagues and friends for the inclusive environment, and all the fun times at the office, during teaching and on weekends. Finally, I would like to thank my family and most importantly Monica; for her love, support and patience.

List of publications

This thesis is based on the following publications:

[A] **V. Tu**, L.E. Asp, N. Shirshova, F. Larsson, K. Runesson, R. Jänicke, "Performance of bicontinuous structural electrolytes". *Multifunctional Materials*, vol. 3, 2020, 025001.

[B] **V. Tu**, F. Larsson, K. Runesson, R. Jänicke, "Variationally consistent homogenization of ion transport in an electrochemical system". *Manuscript to be submitted for publication.*

Other publications related to thesis:

D. Carlstedt, K. Runesson, F. Larsson, **V. Tu**, R. Jänicke, L.E. Asp, "Computational modelling of structural batteries accounting for stress-assisted convection in the electrolyte". *International Journal of Solids and Structures*, vol. 238, 2022, 111343.

Contents

Part I

Extended summary

CHAPTER 1

Introduction

1.1 Background

A vital decarbonization strategy is the vehicle electrification of road-based transportation [1]. The electric vehicle (EV) sales reached an all-time high of 6.6 million in 2021, representing nearly 9% of the global car sales [2, 3]. However, much still remains in order to meet the projected requirement of 300 million electric cars on the road by 2030 related to the "Net Zero Emissions Scenario by 2050" set up by the International Energy Agency (IEA) [4]. There are various factors (demographic, technical, cost, governmental, psychological etc.) influencing consumers' willingness to purchase battery electric vehicles (BEVs) [5]. In the context of technical features, one of the largest technological barriers that is preventing consumers from purchasing BEVs is the limited driving range [1, 5]. One way to improve this is by increasing the specific energy (Wh kg^{-1}) stored in the vehicle. Hence, there is a need for energy storage solutions that can provide significant system mass and volume savings in order to not only extend the driving range of EVs, but also enable other forms of sustainable transportation such as electric aviation [6].

Aside from further advancing existing electrochemical energy storage tech-

nologies, an alternative strategy is to develop the so-called "structural battery". Unlike conventional monofunctional batteries that can only store and deliver energy, the structural battery is multifunctional in the sense that it is able to carry mechanical loads, and at the same time store and deliver energy [7, 8]. This technology relies on the carbon fiber's reversible lithium insertion capability [9] and its intrinsic ability to conduct current and carry tensile loads. Indeed, by fully utilizing all of the carbon fibers' capabilities, it becomes possible to exploit them as structural battery electrodes [10, 11]. Note here that it is only the negative electrodes that the carbon fibers can directly function as. In order to work as positive electrodes, the carbon fibers first need to be coated with lithium metal oxide or olivine based particles, e.g. $LiFePO_4$, binder and conductive additives [12–14].

While conventional batteries rely solely on liquid electrolyte to allow for ion transfer between the electrodes, the structural battery exploits the so-called structural battery electrolyte (SBE) [15–17]. The SBE consists of two continuous phases; a nanoporous polymer skeleton and a liquid electrolyte. The role of the liquid electrolyte is to allow for ion transfer, while the porous polymer skeleton contributes to the mechanical properties. In short, each constituent of the structural battery is designed to be multifunctional and utilized to its fullest potential, hence ensuring that significant weight and volume savings are achieved [7, 8, 18]. So far, the most widespread structural battery architectures are the laminated version and the so-called "3D-battery" (also micro-battery) [7, 8]. In this thesis, the focus will be on the laminated architecture, see Figure 1.1.

The complexity of structural batteries give rise to numerous challenges that need to be overcome. A major challenge in producing high-performing structural batteries lies in the design and performance prediction of SBEs [7, 8]. In order to truly optimize the design w.r.t. the multifunctional performance, there is a need for modeling tools that can contribute to advancing SBE research.

Plenty of research has been performed in modeling of electrochemical systems. Newman et al. were one of the first groups to develop numerical models of coupled electrochemical reaction-diffusion in batteries [19–21]. Additionally, we note the works by Samson et al. [22], Danilov and Notten [23], Dickinson et al. [24], and Bauer et al. [25] to name a few. Regarding multiscale modeling of electrochemical systems, we note that Salvadori and co-workers worked on the

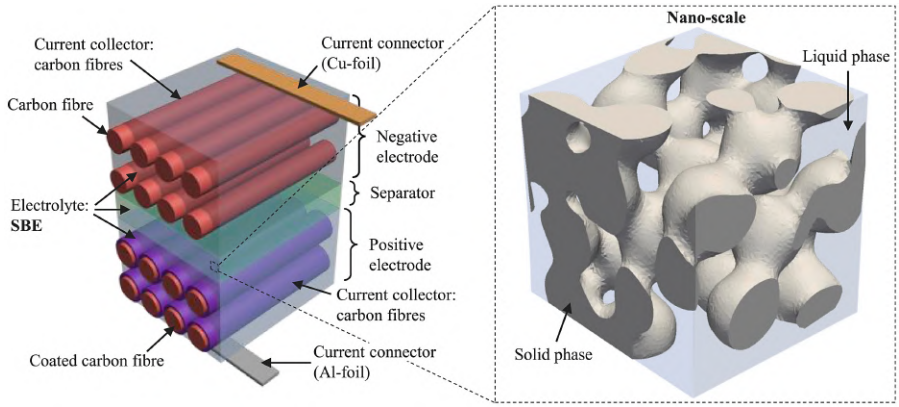

Figure 1.1: Schematic illustration of the laminated structural battery (left image). Artificially generated RVE (right image) representing the microstructure of the SBE that consists of a polymer skeleton and a liquid electrolyte. From Carlstedt et al. [30].

multiscale analysis of electrochemical systems [26, 27]. During recent years, we have also seen modeling works related to structural batteries emerge. Xu et al. [28] worked on multiphysics modeling of a single carbon fiber micro-battery. Carlstedt et al. [29–31] worked with structural battery modeling with emphasis on the multiphysics couplings, e.g. thermo–electro–chemo–mechanical and even accounted for stress-assisted convection in the SBE.

1.2 Research scope

A major part of existing battery research focuses on 1D single scale modeling, where the consideration of underlying microstructure effects are limited. Due to multi-physics phenomena (ion transport in nanoporous materials, electrode kinetics etc.) taking place several orders of magnitude below the battery cell size, it is clear that computational modeling of batteries is inherently multiscale in space and time [32]. Therefore, the long term goal of this project is to develop a multiscale modeling framework for structural batteries. In order to achieve this, the following sub-goals are identified:

(i) Develop methods to numerically generate 3D Representative Volume

Elements (RVEs) representing the SBE microstructures. Virtual material tests can then be used to assess the performance of various SBE microstructure morphologies. This topic is investigated in Paper A.

(ii) Develop a multiscale modeling framework for electrochemically coupled ion transport in SBEs. Paper B is dedicated to this topic.

In Paper A, the artificial RVE generation is performed with limited ability to account for microstructure features such as pore size distribution and tortuosity. Furthermore, numerical investigations compared the mechanical and transport properties (assuming linear constitutive relations) for a variety of SBE microstructure morphologies. The ion transport was modeled using Fick's law; hence, the more elaborate electrochemical formulation involving both migration (caused by electric field) and diffusion of ions was not considered. In Paper B, the ion transport formulation was extended to include both migration and diffusion. A rigorous treatment of electromagnetism (to model ionic migration) would require involving Maxwell's equations, but by making the critical assumption that the magnetic field is assumed to vary slowly, the formulation is simplified to electrostatics. In such a case, the electrochemical ion transport can be established by coupling Gauss' law with a mass conservation law for each chemical species.

So far, only the ion transport[1]in the SBE has been studied in Paper A and Paper B. Obviously, the structural battery simulations can not be performed without a rigorous description of the electrodes and coupling to the mechanical field. A discussion on how this topic will be handled in future work is found in Section 5.

[1]Although the mechanical problem is scarcely treated in this thesis, the thesis still falls within the bounds of solid and structural mechanics. Despite investigating governing equations from various branches of physics, the numerical methods and modeling techniques are general.

CHAPTER 2

Structural electrolytes

2.1 Synthesis

The structural battery is a type of structural power composite; another innovation that also falls into this category is the structural supercapacitor. Although the innovations are different, they do share the same challenges when it comes to the structural electrolyte; i.e. it is required to have high ionic conductivity while providing mechanical integrity [7]. In this section, we will consider structural electrolyte morphologies made for structural batteries as well as structural supercapacitors.

The two main methods for synthesis of (in-situ liquid filled) structural electrolytes are high internal phase emulsion (HIPE) templating [15] and polymerization induced phase separation (PIPS) [16, 17]. The HIPE templating approach mixes two immiscible phases to form an emulsion. Polymerization around emulsion droplets result in the formation of highly porous polymers. The PIPS method exploits components with specific solubility parameters. Initially, they might be fully miscible, but later on, they become immiscible as the monomers transform into polymers. Scanning electron microscope (SEM) images of several electrolyte systems based on both HIPE templating

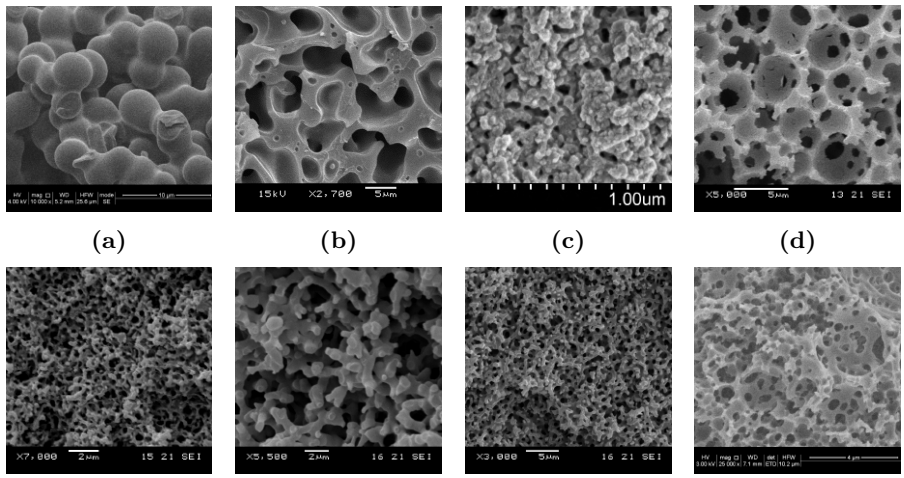

Figure 2.1: SEM images of various structural electrolytes (solid polymer matrix); (a) 60DGEBA, (b) 50MTM57/2.3M_1PC, (c) AB/0.65, (d) polyHIPE, (e) 50VTM266/2.3M, (f) 30MVR444/2.3M, (g) 40MVR444/2.3M, and (h) polyMIPE. The names of the samples refer to their chemical composition and manufacturing method. Subfigure (c) from [16], rest from [33].

and PIPS are shown in Figure 2.1.

2.2 Artificial RVE generation

The Representative Volume Element (RVE) is a vital part of multiscale modeling since it contains information of the underlying microstructure. In a two-scale model, the macroscale problem depends on the homogenization of the subscale RVE problem. Due to the complexity in obtaining and working with real 3D data of SBEs (e.g. from focused ion beam and SEM), an alternative approach is to numerically generate simplified RVEs for numerical analysis. This strategy is pursued in Paper A.

In this section, we attempt to generate some classes of periodic and bicontinuous microstructures that seem reasonable based on the collection of SEM images in Figure 2.1. Most of the generation techniques involve tampering with various Boundary Value Problems (BVP) to obtain solution fields that

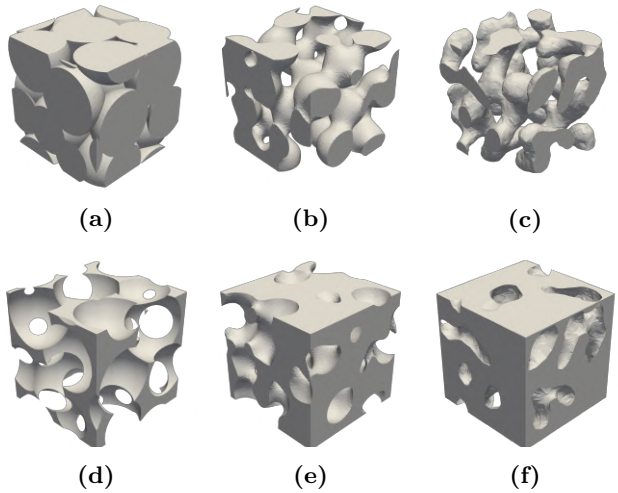

Figure 2.2: Solid polymer matrix of various artificially generated microstructures; (a) bead, (b) trabecular, (c) imperfect trabecular, (d) inverse bead, (e) inverse trabecular, and (f) inverse imperfect trabecular.

can be converted to meshable solids. An extensive overview on generation of random microstructures, with emphasis on bicontinuous mixtures, is available in Bargmann et al. [34, 35].

In this project, the following microstructure classes are generated:

(i) Bead structures: A dense sphere packing, with uniform particle size, is obtained by exploiting the Lubachevsky-Stillinger algorithm [36, 37]. In the next step, the radius is increased until the spheres overlap. The amount of overlap controls the porosity of the resulting structure within certain limits. The resulting 3D microstructures are porous and bicontinuous; resembling a structure built of sintered beads, see Figure 2.2a.

(ii) Trabecular structures: A periodic 3D Voronoi tesselation [38] with uniform cells is inserted into a smooth cube. The intersection of the Voronoi tesselation and the smooth cube results in periodic Voronoi cells enclosed in the cube. This is used as the input geometry for solving a fictitious linear stationary heat equation (in fact, any generic Poisson's equation)

in the form as follows

$$\Delta\varphi = f \quad \text{in } \Omega, \tag{2.1}$$

where φ is a scalar field and f is a source term. Here, the edges of the Voronoi cells are constrained as heat sources, while the centers of the cells (seed points) are constrained as heat sinks. Additionally, periodic boundary conditions are exploited.

From the resulting 3D temperature distribution, isosurfaces at fixed temperature levels can (together with corresponding "isovolumes") be extracted and converted into meshable 3D solid structures, see Figure 2.2b. The final structures, denoted trabecular, are bicontinuous with interconnected pore channels. The porosity of the structure is controlled by varying the temperature level. The microstructure generation procedure is outlined in Figure 2.3.

(iii) Imperfect trabecular structures: This type of microstructure is obtained by solving the Cahn-Hilliard equation [39, 40] in the form as follows

$$\partial_t \phi + \boldsymbol{q}_\mu \cdot \boldsymbol{\nabla} = 0 \quad \text{in } \Omega, \tag{2.2}$$

$$(\phi^3 - \phi - \mu) + \boldsymbol{q}_\phi \cdot \boldsymbol{\nabla} = 0 \quad \text{in } \Omega, \tag{2.3}$$

with the constitutive relations

$$\boldsymbol{q}_\mu := -M\boldsymbol{\nabla}\mu, \tag{2.4}$$

$$\boldsymbol{q}_\phi := -\gamma\boldsymbol{\nabla}\phi. \tag{2.5}$$

where ϕ represents the concentration difference between different phases, μ the chemical potential, M the mobility, and γ related to the thickness of transition regions. Periodic boundary conditions are used.

These microstructures tend to be more irregular with pore channels that are not fully connected; the microstructure is only partly bicontinuous. There are both dead-end channels as well as some unconnected pores. Hence, we coin the name imperfect trabecular structures. The porosity of the imperfect trabecular structures is controlled by adjusting the magnitude of the initial condition to the Cahn-Hilliard equation. See Figure 2.4 for the microstructure generation procedure.

(iv) Inverted microstructures: Although this is not a truly distinct microstructure class, we reuse all microstructures by inverting them, see Figure 2.2d-2.2f. This results in the inverted bead structure, the inverted trabecular structure and the inverted imperfect trabecular structure.

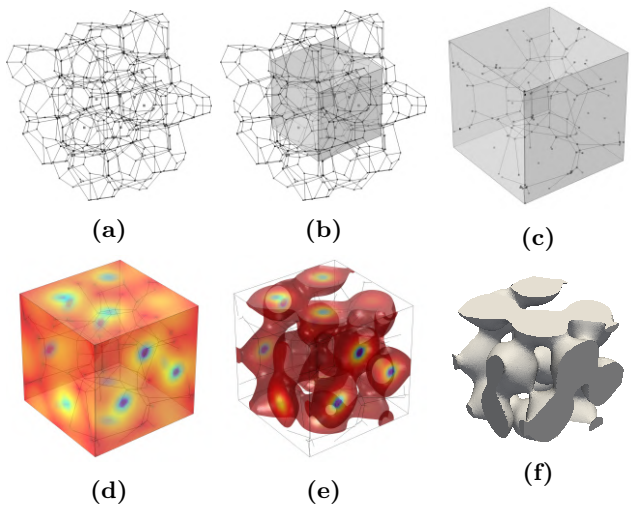

Figure 2.3: Sequential steps for generation of trabecular structures; (a) periodic Voronoi tessellation, (b) embedding Voronoi tessellation in a cube, (c) constraints on a periodic network inside a cube, (d) temperature field of fictitious heat equation, (e) filtered temperature field, and (f) conversion to meshable solid.

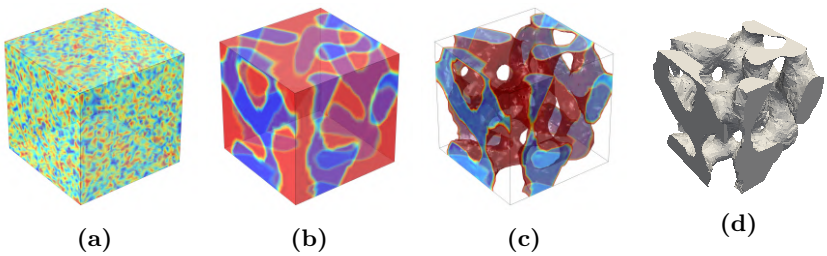

Figure 2.4: Sequential steps for generation of imperfect trabecular structures; (a) noise distribution as initial condition, (b) solution field ϕ of Cahn-Hilliard equation, (c) filtered solution field, (d) conversion to meshable solid.

2.3 Virtual material testing

In this section, virtual testing is exploited on the artificially generated microstructures to derive the effective material properties that characterize the macroscopic response. Subscale quantities in the RVE domain $\Omega_\square$ are homogenized via the RVE volume averaging operator as follows

$$\langle \bullet \rangle_\square := \frac{1}{|\Omega_\square|} \int_{\Omega_\square} \bullet \, \mathrm{d}\Omega. \tag{2.6}$$

Elastic stiffness

In the simplest possible approach, the absence of pore pressure is assumed together with linear constitutive relations. This corresponds to characterizing mechanical properties of a drained microstructure (only solid phase $\Omega_{\square,\mathrm{S}}$). In the absence of body forces, linear elasticity on the subscale (with suitable boundary conditions) is defined as

$$-\boldsymbol{\sigma} \cdot \boldsymbol{\nabla} = \mathbf{0} \quad \text{in } \Omega_{\square,\mathrm{S}}, \tag{2.7a}$$

$$\boldsymbol{\sigma} = \mathbf{E} : \boldsymbol{\epsilon}, \tag{2.7b}$$

with the stress $\boldsymbol{\sigma}$, the strain $\boldsymbol{\epsilon}$, and the isotropic stiffness tensor $\mathbf{E}$ representing the (intrinsic) stiffness of the solid polymer phase. The elastic parameters in $\mathbf{E}$ are chosen as Young's modulus E and Poisson's ratio ν.

The goal is to compute the effective stiffness tensor $\bar{\mathbf{E}}$ of the porous solid phase via the macroscopic relation

$$\bar{\boldsymbol{\sigma}} = \bar{\mathbf{E}} : \bar{\boldsymbol{\epsilon}}, \tag{2.8}$$

with the effective strain $\bar{\boldsymbol{\epsilon}}$, and the (post-processed) effective stress $\bar{\boldsymbol{\sigma}} := \langle \boldsymbol{\sigma} \rangle_\square$ revealing the overall stiffness of the porous RVE.

Clearly, the subscale RVE problem needs to be solved in order to compute $\bar{\mathbf{E}}$. The first step is to introduce the classical assumption of first order homogenization as

$$\boldsymbol{u}(\boldsymbol{x}) = \bar{\boldsymbol{\epsilon}} \cdot \boldsymbol{x} + \boldsymbol{u}^{\mathrm{S}}(\boldsymbol{x}). \tag{2.9}$$

where $\boldsymbol{x}$ is the position in the RVE domain, $\boldsymbol{u}$ is the subscale displacement field, and $\boldsymbol{u}^{\mathrm{S}}$ is a periodic fluctuation field (from prescribing periodic bound-

ary conditions) in the RVE. The macroscopic strain $\bar{\boldsymbol{\epsilon}}$ allows the macroscale problem to interact with the subscale problem, and serves as the "input loading" to the RVE. Furthermore, note that a centered RVE is assumed, and that $\bar{\boldsymbol{u}} = \mathbf{0}$ since it simply represents a rigid body motion.

From here on, the subscale is solved by imposing the six independent loading cases of the symmetric macroscopic strain tensor $(\bar{\boldsymbol{\epsilon}})_{kl}$ with $k, l = 1, 2, 3$. Finally, the components $(\bar{\mathbf{E}})_{ijkl}$ (with $i, j, k, l = 1, 2, 3$) of the macroscopic elasticity tensor can be computed from the macroscopic response $\langle(\boldsymbol{\sigma})_{ij}\rangle_{\square}$ of the RVE under the macroscopic unit strain $(\bar{\boldsymbol{\epsilon}})_{kl} = 1$ via the relation

$$(\bar{\mathbf{E}})_{ijkl} = \frac{\partial\langle(\boldsymbol{\sigma})_{ij}\rangle_{\square}}{\partial(\bar{\boldsymbol{\epsilon}})_{kl}} := \langle(\boldsymbol{\sigma})_{ij}\rangle_{\square}\Big|_{(\bar{\boldsymbol{\epsilon}})_{kl}=1}. \tag{2.10}$$

Ionic conductivity

Under the assumption that chemical diffusion only occurs in the liquid electrolyte phase of the SBE $\Omega_{\square,\mathrm{E}}$, and that convection can be neglected; the linear stationary Fickian diffusion on the subscale (with suitable boundary conditions) is defined as

$$-\boldsymbol{j} \cdot \boldsymbol{\nabla} = 0 \quad \text{in } \Omega_{\square,\mathrm{E}}, \tag{2.11a}$$

$$\boldsymbol{j} := -M\,\boldsymbol{g}, \tag{2.11b}$$

where $\boldsymbol{j}$ is the ion mass flux, $\boldsymbol{g} := \boldsymbol{\nabla}\mu$ is the gradient of the chemical potential μ, and M is the intrinsic isotropic ionic conductivity of the liquid electrolyte.

In the same fashion as the elastic problem, the aim is to compute the effective ionic conductivity tensor $\bar{\boldsymbol{M}}$ via the macroscopic relation

$$\bar{\boldsymbol{j}} := -\bar{\boldsymbol{M}} \cdot \bar{\boldsymbol{g}}, \tag{2.12}$$

where $\bar{\boldsymbol{g}} := \boldsymbol{\nabla}\bar{\mu}$ and the effective (post-processed) ionic mass flux $\bar{\boldsymbol{j}} := \langle\boldsymbol{j}\rangle_{\square}$. Due to the heterogeneous distribution of the pore space in the RVE, $\bar{\boldsymbol{M}}$ might be anisotropic in contrast to the isotropic conductivity M of the liquid electrolyte.

Once again, first order homogenization is introduced as

$$\mu(\boldsymbol{x}) = \bar{\boldsymbol{g}} \cdot \boldsymbol{x} + \mu^{\mathrm{S}}(\boldsymbol{x}). \tag{2.13}$$

Finally, the subscale problem is solved by imposing the three independent loading cases of the gradient vector $(\bar{\boldsymbol{g}})_n$ with $n = 1, 2, 3$. The components $(\bar{\boldsymbol{M}})_{mn}$ (with $m, n = 1, 2, 3$) of the overall conductivity tensor can be computed from the RVE response $\langle(\boldsymbol{j})_m\rangle_\square$ of the RVE under the macroscopic unit gradient $(\bar{\boldsymbol{g}})_n = 1$ of the chemical potential via the relation

$$(\bar{\boldsymbol{M}})_{mn} = -\frac{\partial\langle(\boldsymbol{j})_m\rangle_\square}{\partial(\bar{\boldsymbol{g}})_n} := -\langle(\boldsymbol{j})_m\rangle_\square\Big|_{(\bar{\boldsymbol{g}})_n=1}. \tag{2.14}$$

Remark. The effective ionic conductivity computation can trivially be extended to include both chemical diffusion and ionic migration due to an electric field. The variable μ can simply be reinterpreted as the electrochemical potential $\mu := \hat{\mu} + Fz\varphi$, where $\hat{\mu}$ is now the chemical potential and φ is the electric potential. Additionally, F is Faraday's constant and z is the charge number for e.g. Li-ions ($z = +1$). In fact, this holds even for the simplified balance equation (Fickian diffusion) since the effective ionic conductivity only depends on the subscale ionic flux $\boldsymbol{j} := -M\,\boldsymbol{g}$. Obviously, this is true only upon making the critical model assumption that the ionic conductivity is the same whether it is the electric or the chemical potential gradient that is the driving force. This strategy is pursued in Paper A. □

Quasi-isotropic properties

A limitation of the proposed artificial RVE generation technique lies in the limited RVE size and, therefore, the statistical representation of microstructure features. The computed effective stiffness tensors $\bar{\mathbf{E}}$ and ionic conductivity tensors $\bar{\boldsymbol{M}}$ might contain some anisotropy; hence, we compute quasi-isotropic scalar values for $\bar{E}$ and $\bar{M}$.

There are several ways to do this; however, in Paper A, the effective bulk modulus $\bar{K}$ and the effective shear modulus $\bar{G}$ are computed as follows

$$\bar{G} := \frac{1}{3}[(\bar{\mathbf{E}})_{1212} + (\bar{\mathbf{E}})_{1313} + (\bar{\mathbf{E}})_{2323}], \tag{2.15}$$

$$\bar{K} := \frac{1}{3}[(\bar{\mathbf{E}})_{1122} + (\bar{\mathbf{E}})_{1133} + (\bar{\mathbf{E}})_{2233}] + \frac{2}{3}\bar{G}. \tag{2.16}$$

In the next step, the quasi-isotropic Young's modulus is obtained as

$$\bar{E} = \frac{9\bar{K}\bar{G}}{3\bar{K} + \bar{G}}. \tag{2.17}$$

Finally, the quasi-isotropic ionic conductivity is computed as

$$\bar{M} \coloneqq \frac{1}{3}[(\bar{\boldsymbol{M}})_{11} + (\bar{\boldsymbol{M}})_{22} + (\bar{\boldsymbol{M}})_{33}]. \tag{2.18}$$

CHAPTER 3

Multiscale modeling of electrochemical systems

3.1 Governing equations

This section treats the balance equations of the electrochemically coupled transient transport of electroactive species in the SBE. Additionally, the relevant constitutive relations in the liquid electrolyte domain Ω_{E} and the solid polymer domain Ω_{S} are defined. Although all equations pertaining to ion transport are valid for any number of ions $\alpha = 1, 2, \ldots, N$, the considered electrochemical system will in practice consist of Li-ions (Li^+) and a corresponding companion anion (e.g. PF_6^-) that is simply denoted X^-.

A rigorous treatment of electromagnetism (to model ionic migration) would require involving Maxwell's equations, but by making the critical assumption that the magnetic field is assumed to vary slowly, the formulation is simplified to electrostatics where the electric field conveniently depends solely on the electric potential gradient. For electrochemical systems that involve N mass balance equations (one for each species), the number of unknowns becomes $N + 1$ due to N chemical potentials and one electric potential. Therefore, an additional equation is required; the most common choice in battery modeling is the assumption of electroneutrality [32].

Balance equations

Assuming once again a biphasic material such as the SBE, and exploiting the assumption of electroneutrality $\sum_\alpha z_\alpha c_\alpha = 0$ results in the following formulation

$$\boldsymbol{i} \cdot \boldsymbol{\nabla} = 0 \quad \text{in } \Omega_\mathrm{E} \times (0, T], \tag{3.1a}$$

$$\partial_\mathrm{t} c_\alpha + \boldsymbol{j}_\alpha \cdot \boldsymbol{\nabla} = 0 \quad \text{in } \Omega_\mathrm{E} \times (0, T], \tag{3.1b}$$

with suitable boundary conditions, constitutive relations, and initial conditions. Here, the first equation represents charge conservation under electroneutrality assumption while the second equation expresses mass conservation for species α. The quantity $\boldsymbol{i}$ is the current density, c_α the molar concentration, and $\boldsymbol{j_\alpha}$ the ion mass flux.

However, since electroneutrality is not a fundamental law, it can lead to paradoxes in certain situations. Dickinson et al. [24] showed that electroneutrality is not automatically consistent with Maxwell's equations; especially the electric field can become erroneous [23]. A more correct formulation is to replace the electroneutrality condition with Gauss' law [41]; this will not only give a better prediction of the electric field, but also be able to resolve the electric potential in the solid phase of a biphasic material.

Hence, restricting to electrostatics, we seek the electric potential $\varphi(\boldsymbol{x}, t)$ and the chemical potentials $\mu_\alpha(\boldsymbol{x}, t)$, $\alpha = 1, 2, \ldots, N$, that solve the system

$$\rho - \boldsymbol{d} \cdot \boldsymbol{\nabla} = 0 \quad \text{in } \Omega \times (0, T], \tag{3.2a}$$

$$\partial_\mathrm{t} c_\alpha + \boldsymbol{j}_\alpha \cdot \boldsymbol{\nabla} = 0 \quad \text{in } \Omega_\mathrm{E} \times (0, T], \tag{3.2b}$$

with suitable boundary conditions, constitutive relations, and the initial condition

$$c_\alpha(\bullet, 0) = c_{\alpha,0} \quad \text{in } \Omega_\mathrm{E}. \tag{3.3}$$

Here, the first equation represents Gauss' law which (unlike electroneutrality) properly describes the electric field. The quantity ρ is the free charge density (per unit volume) and $\boldsymbol{d}$ is the electric flux density (electric displacement field).

Constitutive relations

The electric flux density $\boldsymbol{d}$ and the ion mass flux $\boldsymbol{j}_\alpha$ are defined as

$$\boldsymbol{d} := \boldsymbol{\epsilon} \cdot \boldsymbol{E}, \quad \boldsymbol{E}[\varphi] := -\boldsymbol{\nabla}\varphi, \tag{3.4a}$$

$$\boldsymbol{j}_\alpha := -\boldsymbol{M}_\alpha \cdot [\boldsymbol{\nabla}\mu_\alpha + z'_\alpha \boldsymbol{\nabla}\varphi], \tag{3.4b}$$

where φ is the electric potential and μ_α the chemical potential of a mobile species ($\alpha = 1, 2, \ldots, N$) with the ionic charge $z'_\alpha = F z_\alpha$. Here, F corresponds to the Faraday constant and z_α is the valancy of species α. The material properties are given as the electric permittivity $\boldsymbol{\epsilon}$ and the ionic mobility $\boldsymbol{M}_\alpha$ of species α. In the simple case of material isotropy, they can be condensed to the scalar electric permittivity ϵ and the scalar ionic mobility M_α.

Additionally, the free charge density ρ and the molar concentration c_α are defined as

$$\rho := \begin{cases} \sum_{\alpha=1}^{N} z'_\alpha c_\alpha & \text{in } \Omega_\mathrm{E}, \\ 0 & \text{in } \Omega_\mathrm{S}, \end{cases} \tag{3.5a}$$

$$c_\alpha := c_\alpha(\{\mu_\beta\}_{\beta=1}^{N}) \qquad \text{in } \Omega_\mathrm{E}. \tag{3.5b}$$

In the simplest approach, we assume a dilute distribution of charged ions in the electrolyte. Thus, the concentration c_α can be computed from the chemical potential μ_α as follows

$$\mu_\alpha = \mu_{\alpha,0} + RT \ln(\gamma_\alpha c_\alpha), \tag{3.6}$$

where $\mu_{\alpha,0}$ is the reference chemical potential of species α, R the gas constant, T the temperature and γ_α the activity coefficient of species α. If the concentration is assumed to have small fluctuations around the concentration level $c_\alpha = c_{\alpha,0}$, then the relation (3.6) can be linearized. Linearization of (3.6) around $c_\alpha = c_{\alpha,0}$ with the assumption $\mu_{\alpha,0} = -RT \ln(\gamma_\alpha c_{\alpha,0})$ results in the relation

$$c_\alpha = k_\alpha \mu_\alpha + c_{\alpha,0}, \tag{3.7}$$

where k_α depends on the choice of γ_α. Choosing γ_α such that it is constant results in the simple relation $k_\alpha = \frac{c_{\alpha,0}}{RT}$.

Finally, the current density in the electrochemical system can be computed

via Faraday's rule of electrolysis as a post-processing quantity as

$$\boldsymbol{i} := \sum_{\alpha=1}^{N} z'_\alpha \boldsymbol{j}_\alpha. \tag{3.8a}$$

Weak formulation of fine-scale problem

With the governing equations established, the corresponding weak formulation at every time instance reads: find $(\varphi, \mu_\alpha) \in \mathbb{P} \times \mathbb{M}_\alpha$ that solve

$$\int_\Omega \delta\varphi\, \rho \,\mathrm{d}\Omega + \int_\Omega \boldsymbol{\nabla}\delta\varphi \cdot \boldsymbol{d} \,\mathrm{d}\Omega = \int_{\Gamma_{\mathrm{N}}^{(\varphi)}} \delta\varphi\, d^{\mathrm{p}} \,\mathrm{d}\Gamma \qquad \forall \delta\varphi \in \mathbb{P}^0, \tag{3.9a}$$

$$\int_{\Omega_{\mathrm{E}}} \delta\mu_\alpha\, \partial_{\mathrm{t}} c_\alpha \,\mathrm{d}\Omega - \int_{\Omega_{\mathrm{E}}} \boldsymbol{\nabla}\delta\mu_\alpha \cdot \boldsymbol{j}_\alpha \,\mathrm{d}\Omega = -\int_{\Gamma_{\mathrm{N}}^{(\alpha)}} \delta\mu_\alpha\, j_\alpha^{\mathrm{p}} \,\mathrm{d}\Gamma \qquad \forall \delta\mu_\alpha \in \mathbb{M}_\alpha^0, \tag{3.9b}$$

for $\alpha = 1, 2, \ldots, N$ and appropriately defined initial conditions. Here, Neumann boundary conditions $\boldsymbol{d} \cdot \boldsymbol{n} := d^{\mathrm{p}}$ and $\boldsymbol{j}_\alpha \cdot \boldsymbol{n} := j_\alpha^{\mathrm{p}}$ are prescribed on $\Gamma_N^{(\varphi)}$ and $\Gamma_N^{(\alpha)}$ respectively. Exact definitions of the trial and test spaces are left out for brevity.

3.2 Variationally consistent homogenization

So far, only the fine-scale (single-scale) problem has been established. However, performing Direct Numerical Simulations (DNS) to account for microstructure features (e.g. SBE pores) that are several orders of magnitude smaller than the component level (e.g. battery scale) is computationally infeasible. As a consequence, numerous multiscale methods that provide more efficient solution strategies have been developed; see Multiscale Finite Element Method (MsFEM) [42], Heterogeneous Multiscale Methods (HMM) [43], and Variational MultiScale (VMS) [44] to name a few.

In this thesis, the concept of Variationally Consistent Homogenization (VCH) [45] is adopted. As a result, a smooth macroscale problem and a subscale RVE problem can be deduced solely from the fine-scale problem. The steps required in order to achieve this are as follows:

(i) Introduce the running average approximation

$$\int_\Omega \bullet \, \mathrm{d}\Omega \approx \int_\Omega \langle \bullet \rangle_\square(\bar{\boldsymbol{x}}) \, \mathrm{d}\Omega \quad \bar{\boldsymbol{x}} \in \Omega, \tag{3.10}$$

where all fine-scale quantities ($\forall\, \bar{\boldsymbol{x}} \in \Omega$) are approximated as the volume average (over $\Omega_\square$) in the RVE. Here, the RVE domain is assumed to be centered at $\bar{\boldsymbol{x}}$.

(ii) Assume scale separation via first order homogenization

$$\varphi(\bar{\boldsymbol{x}}; \boldsymbol{x}, t) = \bar{\varphi}(\bar{\boldsymbol{x}}, t) + \boldsymbol{\nabla}\bar{\varphi}(\bar{\boldsymbol{x}}, t) \cdot [\boldsymbol{x} - \bar{\boldsymbol{x}}] + \varphi^{\mathrm{S}}(\bar{\boldsymbol{x}}; \boldsymbol{x}, t) \tag{3.11a}$$

$$\mu_\alpha(\bar{\boldsymbol{x}}; \boldsymbol{x}, t) = \bar{\mu}_\alpha(\bar{\boldsymbol{x}}, t) + \boldsymbol{\nabla}\bar{\mu}_\alpha(\bar{\boldsymbol{x}}, t) \cdot [\boldsymbol{x} - \bar{\boldsymbol{x}}] + \mu^{\mathrm{S}}_\alpha(\bar{\boldsymbol{x}}; \boldsymbol{x}, t) \tag{3.11b}$$

where the decomposition corresponds to a first order Taylor expansion $\bar{\bullet}(\bar{\boldsymbol{x}}, t) + \boldsymbol{\nabla}\bar{\bullet}(\bar{\boldsymbol{x}}, t) \cdot [\boldsymbol{x} - \bar{\boldsymbol{x}}]$ around $\bar{\boldsymbol{x}}$ and a fluctuation field $\bullet^{\mathrm{S}}(\bar{\boldsymbol{x}}; \boldsymbol{x}, t)$. Henceforth, the notation on the explicit choice of RVE at macroscale position $\bar{\boldsymbol{x}}$ is left out for brevity. Moreover, the gradients are shortened as $\bar{\boldsymbol{g}}^{\varphi} := \boldsymbol{\nabla}\bar{\varphi}$ and $\bar{\boldsymbol{g}}^{\mu}_\alpha := \boldsymbol{\nabla}\bar{\mu}_\alpha$.

Macroscale problem

The macroscale problem is obtained upon testing with only the macroscopic test functions. Hence, the weak formulation at every time instance reads: find $(\bar{\varphi}, \bar{\mu}_\alpha) \in \bar{\mathbb{P}} \times \bar{\mathbb{M}}_\alpha$ that solve

$$\int_\Omega \delta\bar{\varphi}\, \bar{\rho} + \boldsymbol{\nabla}\delta\bar{\varphi} \cdot \bar{\boldsymbol{\rho}}^{(2)} + \boldsymbol{\nabla}\delta\bar{\varphi} \cdot \bar{\boldsymbol{d}} \, \mathrm{d}\Omega = -\int_{\Gamma^{(\varphi)}_{\mathrm{N}}} \delta\bar{\varphi}\, \bar{d}^{\mathrm{p}} \, \mathrm{d}\Gamma \qquad \forall \delta\bar{\varphi} \in \bar{\mathbb{P}}^0, \tag{3.12a}$$

$$\int_\Omega \delta\bar{\mu}_\alpha\, \partial_{\mathrm{t}}\bar{c}_\alpha + \boldsymbol{\nabla}\delta\bar{\mu}_\alpha \cdot \partial_{\mathrm{t}}\bar{\boldsymbol{c}}^{(2)}_\alpha - \boldsymbol{\nabla}\delta\bar{\mu}_\alpha \cdot \bar{\boldsymbol{j}}_\alpha \, \mathrm{d}\Omega = -\int_{\bar{\Gamma}^{(\mu)}_{\mathrm{N},\alpha}} \delta\bar{\mu}_\alpha\, \bar{j}^{\mathrm{p}}_\alpha \, \mathrm{d}\Gamma \qquad \forall \delta\bar{\mu}_\alpha \in \bar{\mathbb{M}}^0_\alpha, \tag{3.12b}$$

for $\alpha = 1, 2, \ldots, N$ and appropriately defined initial conditions. As a result of VCH, we obtain $\bar{\boldsymbol{\rho}}^{(2)}$ and $\bar{\boldsymbol{c}}^{(2)}_\alpha$ that represent higher order non-standard conservation terms, while the rest are classical averages. Exact definitions of the trial and test spaces are left out for brevity.

Subscale RVE problem

The subscale RVE problem can be obtained upon testing with only the microscopic test functions. However, since the macroscopic parts of the solutions are treated as known loading data to the subscale RVE problem, we may instead seek the full solution as follows: for the given loading histories $\bar{\varphi}(t)$, $\bar{\boldsymbol{g}}^{\varphi}(t)$, $\bar{\mu}_\alpha(t)$, $\bar{\boldsymbol{g}}^{\mu}_\alpha(t)$ at every time instance; find $\varphi \in \mathbb{P}_\square$, $\mu_\alpha \in \mathbb{M}_{\square,\alpha}$, $\lambda^{(\varphi)} \in \mathbb{T}^{(\varphi)}_\square$, $\lambda^{(\mu)}_\alpha \in \mathbb{T}^{(\mu)}_\square$, $\hat{\lambda}^{(\varphi)} \in \mathbb{R}$, $\hat{\lambda}^{(\mu)}_\alpha \in \mathbb{R}$ that solve

$$\langle \delta\varphi\, \rho\rangle_\square + \langle \boldsymbol{\nabla}\delta\varphi \cdot \boldsymbol{d}\rangle_\square - \frac{1}{|\Omega_\square|}\int_{\Gamma^+_\square} [\![\delta\varphi]\!]_\square\, \lambda^{(\varphi)}\,\mathrm{d}\Gamma - \langle\delta\varphi\rangle_\square\,\hat{\lambda}^{(\varphi)} = 0 \qquad \forall \delta\varphi \in \mathbb{P}_\square, \tag{3.13a}$$

$$-\frac{1}{|\Omega_\square|}\int_{\Gamma^+_\square} [\![\varphi]\!]_\square\,\delta\lambda^{(\varphi)}\,\mathrm{d}\Gamma = -\frac{1}{|\Omega_\square|}\int_{\Gamma^+_\square} [\![\boldsymbol{x}]\!]_\square\,\delta\lambda^{(\varphi)}\,\mathrm{d}\Gamma\cdot\bar{\boldsymbol{g}}^{\varphi} \qquad \forall \delta\lambda^{(\varphi)} \in \mathbb{T}^{(\varphi)}_\square, \tag{3.13b}$$

$$-\langle\varphi\rangle_\square\,\delta\hat{\lambda}^{(\varphi)} = -\bar{\varphi}\,\delta\hat{\lambda}^{(\varphi)} \qquad \forall \delta\hat{\lambda}^{(\varphi)} \in \mathbb{R}, \tag{3.13c}$$

$$\phi\,\langle\delta\mu_\alpha\,\partial_{\mathrm{t}} c_\alpha\rangle_{\square,\mathrm{E}} - \phi\,\langle\boldsymbol{\nabla}\delta\mu_\alpha\cdot\boldsymbol{j}_\alpha\rangle_{\square,\mathrm{E}} + \frac{1}{|\Omega_\square|}\int_{\Gamma^+_{\square,\mathrm{E}}} [\![\delta\mu_\alpha]\!]_\square\,\lambda^{(\mu)}_\alpha\,\mathrm{d}\Gamma - \phi\langle\delta\mu_\alpha\rangle_{\square,\mathrm{E}}\,\hat{\lambda}^{(\mu)}_\alpha = 0 \qquad \forall \delta\mu_\alpha \in \mathbb{M}_{\square,\alpha}, \tag{3.13d}$$

$$\frac{1}{|\Omega_\square|}\int_{\Gamma^+_{\square,\mathrm{E}}} [\![\mu_\alpha]\!]_\square\,\delta\lambda^{(\mu)}_\alpha\,\mathrm{d}\Gamma = \frac{1}{|\Omega_\square|}\int_{\Gamma^+_{\square,\mathrm{E}}} [\![\boldsymbol{x}]\!]_\square\,\delta\lambda^{(\mu)}_\alpha\,\mathrm{d}\Gamma\cdot\bar{\boldsymbol{g}}^{\mu}_\alpha \qquad \forall \delta\lambda^{(\mu)}_\alpha \in \mathbb{T}^{(\mu)}_\square, \tag{3.13e}$$

$$-\phi\langle\mu_\alpha\rangle_{\square,\mathrm{E}}\,\delta\hat{\lambda}^{(\mu)}_\alpha = -\phi(\bar{\mu}_\alpha + \bar{\boldsymbol{g}}^{\mu}_\alpha\cdot[\bar{\boldsymbol{x}}_{\mathrm{E}} - \bar{\boldsymbol{x}}])\,\delta\hat{\lambda}^{(\mu)}_\alpha \qquad \forall \delta\hat{\lambda}^{(\mu)}_\alpha \in \mathbb{R}, \tag{3.13f}$$

for $\alpha = 1, 2, \ldots, N$ and appropriately defined initial conditions. Upon enforcing weakly periodic boundary conditions (WPBC) [46], we use the difference operator $[\![\bullet]\!]_\square(\boldsymbol{x}) := \bullet(\boldsymbol{x}) - \bullet(\boldsymbol{x}^-(\boldsymbol{x}))$. Here, $\boldsymbol{x} \in \Gamma^+_\square$ is an image point whereas $\boldsymbol{x}^-(\boldsymbol{x}) \in \Gamma^- = \Gamma_\square \setminus \Gamma^+_\square$ is the corresponding "mirror point". Additionally, while $\langle\bullet\rangle_\square$ is the RVE volume average operator over the full RVE domain, the operator $\langle\bullet\rangle_{\square,\mathrm{E}}$ is restricted to the liquid phase of the SBE. Note that (3.13a)

and (3.13d) correspond to Gauss' law and ion mass conservation, respectively. The rest are constraint equations; (3.13b) and (3.13e) represent WPBCs, while (3.13c) and (3.13f) represent RVE volume average constraints pertaining to proper scale-bridging. Details on the RVE constraints, and exact definitions of the trial and test spaces are left out for brevity.

Solving two-scale models

Two-scale models are often solved via the Finite Element squared (FE^2) method. In this procedure, the macroscale and the subscale RVE problem are solved in a nested fashion with information passing between the scales in both directions. The macroscale solution is sent to the subscale RVE (prolongation), and serves as the driving force ("loading data") to the problem. After solving the subscale RVE problem, effective properties (effective fluxes in VCH) are computed and sent back to the macro-scale (homogenization).

In practice, numerical integration is carried out only at quadrature points; hence, only one subscale RVE computation per macroscopic quadrature point is needed. However, for complex 3D macroscale domains, the number of quadrature points rapidly increases; thus, requiring a large number of subscale RVE computations. Together with the fact that the subscale RVE itself might also be complex, the FE^2 procedure quickly becomes computationally infeasible.

For certain problems, a viable approach is to exploit the assumption of micro-stationarity to enable a priori upscaling. In such a case, the two-scale model is condensed to a macroscale problem with precomputed expressions for effective quantities. This circumvents the need for performing RVE computations at every macroscopic quadrature point for all time steps; instead, the homogenization of the (stationary) RVE is performed once and for all.

3.3 Two-scale model with a priori upscaling

Upon introducing the assumption of micro-stationarity, we may pre-compute expressions for effective fluxes. This allows us to solve a macroscale problem that accounts for the underlying subscale RVE through a priori upscaling. Consider the following split of the subscale RVE solution fields

$$\varphi(\boldsymbol{x},t) = \varphi^{\mathrm{stat}}(\boldsymbol{x},t) + \varphi^{\mathrm{trans}}(\boldsymbol{x},t), \tag{3.14a}$$

$$\mu_\alpha(\boldsymbol{x},t) = \mu_\alpha^{\mathrm{stat}}(\boldsymbol{x},t) + \mu_\alpha^{\mathrm{trans}}(\boldsymbol{x},t), \tag{3.14b}$$

where the (unconventional) notation "stationary" refers to the steady-state response due to sustained loading, while "transient" refers to the response that contains relaxation processes when the loading is applied quickly as compared to the relaxation time.

The stationary solutions can be obtained upon removing all time derivatives from (3.13); the exact formulation of the stationary problem is left out for brevity. However, the stationary solutions can also be computed as a linear combination of sensitivity fields with time-dependent coefficients corresponding to macroscopic load histories. The decomposition of the stationary solutions is performed as follows

$$\begin{aligned}\varphi^{\mathrm{stat}}(\boldsymbol{x},t) &= \varphi_{\bar{\varphi}}(\boldsymbol{x})\,\bar{\varphi}(t) + \boldsymbol{\varphi}_{\bar{g}^\varphi}(\boldsymbol{x})\cdot\bar{\boldsymbol{g}}^\varphi(t) \\ &\quad + \sum_{\alpha=1}^{N}\left(\varphi_{\bar{\mu}_\alpha}(\boldsymbol{x})\bar{\mu}_\alpha(t) + \boldsymbol{\varphi}_{\bar{g}^\mu_\alpha}(\boldsymbol{x})\cdot\bar{\boldsymbol{g}}^\mu_\alpha(t)\right), \end{aligned}\tag{3.15a}$$

$$\begin{aligned}\mu_\alpha^{\mathrm{stat}}(\boldsymbol{x},t) &= \mu_{\alpha,\bar{\varphi}}(\boldsymbol{x})\,\bar{\varphi}(t) + \boldsymbol{\mu}_{\alpha,\bar{g}^\varphi}(\boldsymbol{x})\cdot\bar{\boldsymbol{g}}^\varphi(t) \\ &\quad + \sum_{\beta=1}^{N}\left(\mu_{\alpha,\bar{\mu}_\beta}(\boldsymbol{x})\bar{\mu}_\beta(t) + \boldsymbol{\mu}_{\alpha,\bar{g}^\mu_\beta}(\boldsymbol{x})\cdot\bar{\boldsymbol{g}}^\mu_\beta(t)\right), \end{aligned}\tag{3.15b}$$

where each sensitivity field $[\varphi_{\bar{\varphi}}, \boldsymbol{\varphi}_{\bar{g}^\varphi}, \varphi_{\bar{\mu}_\alpha}, \boldsymbol{\varphi}_{\bar{g}^\mu_\alpha}, \mu_{\alpha,\bar{\varphi}}, \boldsymbol{\mu}_{\alpha,\bar{g}^\varphi}, \mu_{\alpha,\bar{\mu}_\beta}, \boldsymbol{\mu}_{\alpha,\bar{g}^\mu_\beta}]$ is given by each corresponding time-independent unit sensitivity problem; the exact formulations of the unit sensitivity problems are left out for brevity. Based on (3.15), the effective constitutive quantities can be explicitly defined.

For illustration, the effective current density under assumption of micro-stationarity is defined as

$$\bar{\boldsymbol{d}}^{\text{stat}}(\boldsymbol{x},t) = -\langle \boldsymbol{\epsilon}\cdot(\boldsymbol{\nabla}\otimes\boldsymbol{\varphi}_{\bar{g}^{\varphi}})\rangle_{\square}\cdot\bar{\boldsymbol{g}}^{\varphi}(t) - \sum_{\alpha=1}^{N}\langle\boldsymbol{\epsilon}\cdot\boldsymbol{\nabla}\rho_{\bar{\mu}_{\alpha}}\rangle_{\square}\,\bar{\mu}_{\alpha}(t) - \sum_{\alpha=1}^{N}\langle\boldsymbol{\epsilon}\cdot(\boldsymbol{\nabla}\otimes\boldsymbol{\varphi}_{\bar{g}^{\mu}_{\alpha}})\rangle_{\square}\cdot\bar{\boldsymbol{g}}^{\mu}_{\alpha}(t), \tag{3.16}$$

where $\bar{\boldsymbol{g}}^{\varphi}(t)$, $\bar{\mu}_{\alpha}(t)$ and $\bar{\boldsymbol{g}}^{\mu}_{\alpha}(t)$ correspond to known loading data that stem from the macroscale solution. Therefore, the effective quantities simply scale linearly with the "input signals" from the macroscale problem. Remaining effective fluxes, based on micro-stationarity, are left out for brevity.

With all of this, the homogenization of the (stationary) RVE can now be performed once and for all; resulting in an efficient solution scheme of the, otherwise expensive, two-scale model. This strategy is pursued in Paper B.

CHAPTER 4

Summary of included papers

4.1 Paper A

V. Tu, L.E. Asp, N. Shirshova, F. Larsson, K. Runesson, R. Jänicke
Performance of bicontinuous structural electrolytes
Multifunctional Materials, vol. 3, 2020, 025001

In this paper, we study the multifunctional performance of various SBE microstructures by performing virtual material testing on artificially generated representative volume elements (RVE). We attempt to generate some classes of periodic and bicontinuous microstructures that seem to resemble real structural electrolytes. Most of the generation techniques involve tampering with various Boundary Value Problems (BVP) to obtain solution fields that can be converted to meshable solids. The generated microstructure classes are denoted (i) bead structures, (ii) trabecular structures, (iii) imperfect trabecular structures, and (iv) inverted microstructures.

In the next step, virtual material testing is exploited to compute effective material properties. More specifically, the multifunctional performance of artificial RVEs is evaluated in terms of the elastic stiffness and ionic conductivity.

The effective elastic stiffness is computed by homogenizing the subscale RVE problem based on linear elasticity. Here, we make the assumption that the pore pressure in the SBE can be neglected. The effective ionic conductivity is obtained upon homogenizing the subscale RVE problem based on linear stationary Fickian diffusion. Here, we take the simplest approach of neglecting convection.

Upon comparing the multifunctional performance of various artificial RVEs, we identify that the trabecular structures and imperfect trabecular structures perform better than the bead structures.

4.2 Paper B

V. Tu, F. Larsson, K. Runesson, R. Jänicke
Variationally consistent homogenization of ion transport in an electrochemical system
Manuscript to be submitted for publication

This paper covers the development of a multiscale modeling framework for (transient) electrochemically coupled ion transport in SBEs. Unlike classical battery modeling, we avoid the so-called electroneutrality assumption and instead properly resolve the electric field by coupling Gauss' law with mass conservation of chemical species. After establishing the governing equations, we exploit Variationally Consistent Homogenization (VCH) to obtain a two-scale model. Upon formulating the macroscale problem, we are able to reveal higher order non-standard conservation terms due to the VCH approach.

Numerical investigations of the subscale RVE problem show that the micro-transient effects, for length scales relevant to the studied application, are negligible. Therefore, we propose the assumption of micro-stationarity; this opens up for the possibility to devise a numerically efficient two-scale solution scheme based on a priori upscaling. Finally, the paper concludes with computational results for a 2D macro-scale problem based on precomputed effective fluxes from a bicontinuous 3D RVE. Here, we are able to provoke effects of net charge accumulation, which would not be captured upon adopting the classical electroneutrality assumption.

CHAPTER 5

Conclusions and outlook

This thesis treats the multiscale modeling aspects of structural electrolytes. Paper A was dedicated to artificial RVE generation and assessing the multifunctional performance of various SBE microstructures. By tampering with various boundary value problems (heat equationa and Cahn-Hilliard equation), we were able to manipulate the solution fields to resemble SEM images of real structural electrolytes. The solution fields were in turn converted into meshable solids for virtual material testing. Upon assessing multifunctional performance of the artificial RVEs, we concluded that trabecular structures and imperfect trabecular structures perform better than the bead structures. The surprising finding here is that the imperfect trabecular structures perform as well as the trabecular structures. Generation of the trabecular structures is based on prescribing heat sources and heat sinks on a periodic network stemming from a 3D Voronoi tessellation; hence, their microstructures are inherently slightly more controlled and idealized. However, the imperfect trabecular structures are generated by exploiting random noise distributions as initial conditions to the Cahn-Hilliard equation. Owing to the stochastic nature of such RVE generation technique, they have been seen to contain dead-end channels as well as unconnected pores.

Paper A concludes with a comparison of the numerically predicted multifunctional performance of artificial RVEs and experimental data of real structural electrolytes. Unsurprisingly, there is a huge discrepancy between the numerical results and the experimental measurements since the real structural electrolytes contained ionic liquids (supercapacitor application) instead of organic electrolytes (battery application). Moreover, the artificial RVE generation is performed with limited ability to account for microstructure features such as pore size distribution and tortuosity. Currently, the only consistent properties of the artificial RVEs are bicontinuity and periodicity. Furthermore, the virtual material testing of mechanical and transport properties was performed using the simplest possible approach of assuming linear elasticity and Fick's law, respectively. In particular, using Fick's law for ionic liquids is a heavy simplification (i.e. dilute solution theory). While Fickian diffusion models are often used to predict the transport of Li-ions in binary solutions (organic electrolyte), they can not be used to model ion transport in ionic liquids. An example of an organic liquid based binary electrolyte is $LiPF_6$, which contains the ions Li^+ and PF_6^-. However, the ionic liquid used in the experimental data is a mixture of LiTFSI (Li-cation and TFSI-anion) and EMIM-TFSI (EMIM-cation and TFSI-anion), i.e. a so-called ternary system. It has been proposed that such systems are suitably modeled via the Maxwell-Stefan equation which describes the mutual diffusion for a multi-component system [47], and introduces the notion of molecular friction between ions [48]. Nevertheless, the experimental results were kept in Paper A for comparison. Due to the idealized modeling approach of the artificial RVEs, they may serve as an upper-bound for real structural electrolytes in terms of multifunctional performance.

In Paper B, the focus was shifted toward multiscale modeling of electrochemically coupled ion transport processes in SBEs. The ion transport formulation was extended to include both migration and diffusion. Instead of involving Maxwell's equations, the magnetic field was assumed to vary slowly, which simplified the formulation to electrostatics. Hence, the electrochemical ion transport could be established by coupling Gauss' law with a mass conservation law for each chemical species. Moreover, VCH was exploited and a two-scale model was obtained. An efficient two-scale solution scheme was proposed; however the concept relies on the assumption of micro-stationarity. Numerical studies were performed to show that the assumption of micro-

stationarity holds true for time and length scales relevant to the studied application. Finally, the paper concluded with computational results for a 2D macro-scale problem based on precomputed effective fluxes from a bicontinuous 3D RVE. While we were able to provoke net charge accumulation effects using Gauss' law, it should be noted that the employed macroscale boundary conditions do not correspond to a battery application due to the lacking description of the electrodes. In order to properly trace the ions inside the electrodes, a law that describes electrode kinetics such as the Butler-Volmer equation is needed.

As previously mentioned in Section 1.2, only the ion transport in the liquid phase of the SBE has been treated so far. In order to perform full-fledged structural battery simulations, we need a rigorous description of the electrodes and coupling to the mechanical field. Furthermore, due to the high computational cost associated with FE^2 procedures, there is a also a need for general efficient solution schemes that do not rely on assumptions such as microstationarity. Therefore, goals pertaining to future work can be summarized as:

(i) Develop efficient methods for performing multiscale simulations of general electrochemical systems.

(ii) Develop a framework for performing full-fledged multiscale simulations of structural batteries with electro–chemo–mechanical coupling.

In future work, the plan is to treat (i) by exploiting Numerical Model Reduction (NMR), and (ii) by extending Paper B to include the coupled mechanical field and formulate governing equations for the electrodes (including electrode kinetics via the Butler-Volmer equation).

References

[1] Z. P. Cano, D. Banham, S. Ye, A. Hintennach, J. Lu, M. Fowler, and Z. Chen, "Batteries and fuel cells for emerging electric vehicle markets", *Nature Energy*, vol. 3, pp. 279–289, 2018.

[2] EV-volumes. (2022). Global ev sales for 2021, [Online]. Available: `https://www.ev-volumes.com/country/total-world-plug-in-vehicle-volumes` (visited on 04/14/2022).

[3] IEA. (2022). Electric cars fend off supply challenges to more than double global sales, [Online]. Available: `https://www.iea.org/commentaries/electric-cars-fend-off-supply-challenges-to-more-than-double-global-sales` (visited on 04/14/2022).

[4] IEA. (2022). Electric vehicles, [Online]. Available: `https://www.iea.org/reports/electric-vehicles` (visited on 04/14/2022).

[5] W. Li, R. Long, H. Chen, and J. Geng, "A review of factors influencing consumer intentions to adopt battery electric vehicles", *Renewable and Sustainable Energy Reviews*, vol. 78, pp. 318–328, 2017.

[6] A. W. Schäfer, S. R. H. Barrett, K. Doyme, L. M. Dray, A. R. Gnadt, R. Self, A. O'Sullivan, A. P. Synodinos, and A. J. Torija, "Technological, economic and environmental prospects of all-electric aircraft", *Nature Energy*, vol. 4, pp. 160–166, 2019.

[7] L. E. Asp and E. S. Greenhalgh, "Structural power composites", *Composites Science and Technology*, vol. 101, pp. 41–61, 2014.

[8] L. E. Asp, M. Johansson, G. Lindbergh, J. Xu, and D. Zenkert, "Structural battery composites: A review", *Functional Composites and Structures*, vol. 1, p. 042 001, 2019.

[9] R. Kanno, Y. Kawamoto, Y. Takeda, S. Ohashi, N. Imanishi, and O. Yamamoto, "Carbon fiber as a negative electrode in lithium secondary cells", *Journal of The Electrochemical Society*, vol. 139, pp. 3397–3404, 1992.

[10] M. H. Kjell, E. Jacques, D. Zenkert, M. Behm, and G. Lindbergh, "PAN-based carbon fiber negative electrodes for structural lithium-ion batteries", *Journal of The Electrochemical Society*, vol. 158, A1455, 2011.

[11] G. Fredi, S. Jeschke, A. Boulaoued, J. Wallenstein, M. Rashidi, F. Liu, R. Harnden, D. Zenkert, J. Hagberg, G. Lindbergh, P. Johansson, L. Stievano, and L. E. Asp, "Graphitic microstructure and performance of carbon fibre li-ion structural battery electrodes", *Multifunctional Materials*, vol. 1, p. 015 003, 2018.

[12] J. Hagberg, H. A. Maples, K. S. Alvim, J. Xu, W. Johannisson, A. Bismarck, D. Zenkert, and G. Lindbergh, "Lithium iron phosphate coated carbon fiber electrodes for structural lithium ion batteries", *Composites Science and Technology*, vol. 162, pp. 235–243, 2018.

[13] K. Moyer, N. A. Boucherbil, M. Zohair, J. Eaves-Rathert, and C. L. Pint, "Polymer reinforced carbon fiber interfaces for high energy density structural lithium-ion batteries", *Sustainable Energy Fuels*, vol. 4, pp. 2661–2668, 6 2020.

[14] J. S. Sanchez, J. Xu, Z. Xia, J. Sun, L. E. Asp, and V. Palermo, "Electrophoretic coating of lifepo4/graphene oxide on carbon fibers as cathode electrodes for structural lithium ion batteries", *Composites Science and Technology*, vol. 208, p. 108 768, 2021.

[15] N. Shirshova, P. Johansson, M. J. Marczewski, E. Kot, D. Ensling, A. Bismarck, and J. H. G. Steinke, "Polymerised high internal phase ionic liquid-in-oil emulsions as potential separators for lithium ion batteries", *J. Mater. Chem. A*, vol. 1, pp. 9612–9619, 34 2013.

[16] N. Ihrner, W. Johannisson, F. Sieland, D. Zenkert, and M. Johansson, "Structural lithium ion battery electrolytes via reaction induced phase-separation", *J. Mater. Chem. A*, vol. 5, pp. 25 652–25 659, 48 2017.

[17] L. M. Schneider, N. Ihrner, D. Zenkert, and M. Johansson, "Bicontinuous electrolytes via thermally initiated polymerization for structural lithium ion batteries", *ACS Applied Energy Materials*, vol. 2, pp. 4362–4369, 2019.

[18] W. Johannisson, D. Zenkert, and G. Lindbergh, "Model of a structural battery and its potential for system level mass savings", *Multifunctional Materials*, vol. 2, p. 035 002, 2019.

[19] J. Newman and W. Tiedemann, "Porous-electrode theory with battery applications", *AIChE Journal*, vol. 21, pp. 25–41, 1975.

[20] M. Doyle, T. F. Fuller, and J. Newman, "Modeling of galvanostatic charge and discharge of the lithium/polymer/insertion cell", *Journal of The Electrochemical Society*, vol. 140, pp. 1526–1533, 1993.

[21] M. Doyle and J. Newman, "The use of mathematical modeling in the design of lithium/polymer battery systems", *Electrochimica Acta*, vol. 40, pp. 2191–2196, 1995.

[22] E. Samson, J. Marchand, J.-L. Robert, and J.-P. Bournazel, "Modelling ion diffusion mechanisms in porous media", *International Journal for Numerical Methods in Engineering*, vol. 46, pp. 2043–2060, 1999.

[23] D. Danilov and P. Notten, "Mathematical modelling of ionic transport in the electrolyte of li-ion batteries", *Electrochimica Acta*, vol. 53, pp. 5569–5578, 2008.

[24] R. G. C. Edmund J. F. Dickinson Juan G. Limon-Petersen, "The electroneutrality approximation in electrochemistry", *Journal of Solid State Electrochemistry*, vol. 15, pp. 1335–1345, 2011.

[25] G. Bauer, V. Gravemeier, and W. A. Wall, "A stabilized finite element method for the numerical simulation of multi-ion transport in electrochemical systems", *Computer Methods in Applied Mechanics and Engineering*, vol. 223-224, pp. 199–210, 2012.

[26] A. Salvadori, E. Bosco, and D. Grazioli, "A computational homogenization approach for li-ion battery cells: Part 1 – formulation", *Journal of the Mechanics and Physics of Solids*, vol. 65, pp. 114–137, 2014.

[27] A. Salvadori, D. Grazioli, and M. Geers, "Governing equations for a two-scale analysis of li-ion battery cells", *International Journal of Solids and Structures*, vol. 59, pp. 90–109, 2015.

[28] J. Xu, G. Lindbergh, and J. Varna, "Multiphysics modeling of mechanical and electrochemical phenomena in structural composites for energy storage: Single carbon fiber micro-battery", *Journal of Reinforced Plastics and Composites*, vol. 37, pp. 701–715, 2018.

[29] D. Carlstedt, K. Runesson, F. Larsson, J. Xu, and E. Asp, "Electro-chemo-mechanically coupled computational modelling of structural batteries", *Multifunctional Materials*, vol. 3, p. 045 002, 2020.

[30] D. Carlstedt, K. Runesson, F. Larsson, V. Tu, R. Jänicke, and L. E. Asp, "Computational modelling of structural batteries accounting for stress-assisted convection in the electrolyte", *International Journal of Solids and Structures*, vol. 238, p. 111 343, 2022.

[31] D. Carlstedt, K. Runesson, F. Larsson, and L. E. Asp, "On the coupled thermo–electro–chemo–mechanical performance of structural batteries with emphasis on thermal effects", *European Journal of Mechanics - A/Solids*, vol. 94, p. 104 586, 2022.

[32] D. Grazioli, M. Magri, and A. Salvadori, "Computational modeling of li-ion batteries", *Computational Mechanics*, vol. 58, pp. 889–909, 2016.

[33] V. Tu, L. E. Asp, N. Shirshova, F. Larsson, K. Runesson, and R. Jänicke, "Performance of bicontinuous structural electrolytes", *Multifunctional Materials*, vol. 3, p. 025 001, 2020.

[34] S. Bargmann, B. Klusemann, J. Markmann, J. Schnabel, K. Schneider, C. Soyarslan, and J. Wilmers, "Generation of 3d representative volume elements for heterogeneous materials: A review", *Prog. Mater. Sci.*, vol. 96, pp. 322–384, 2018.

[35] C. Soyarslan, S. Bargmann, M. Pradas, and J. Weissmüller, "3d stochastic bicontinuous microstructures: Generation, topology and elasticity", *Acta Mater.*, vol. 149, pp. 326–340, 2018.

[36] B. D. Lubachevsky and F. H. Stillinger, "Geometric properties of random disk packings", *J. Stat. Phys.*, vol. 60, pp. 561–583, 1990.

[37] A. Donev, S. Torquato, and F. Stillinger, "Neighbor list collision-driven molecular dynamics simulation for nonspherical hard particles. i. algorithmic details", *J. Comput. Phys.*, vol. 202, pp. 737–764, 2005.

[38] C. Rycroft, G. Grest, J. Landry, and M. Bazant, "Analysis of granular flow in a pebble-bed nuclear reactor", *Phys. Rev. E*, vol. 74, p. 021 306, 2006.

[39] D. Carolan, H. Chong, A. Ivankovic, A. Kinloch, and A. Taylor, "Co-continuous polymer systems: A numerical investigation", *Comput. Mater. Sci.*, vol. 98, pp. 24–33, 2015.

[40] C. Grant, "Spinodal decomposition for the cahn-hilliard equation", *Commun. Part. Diff. Eq.*, vol. 18, pp. 453–490, 1993.

[41] J. Newman and K. Thomas-Alyea, *Electrochemical Systems*, ser. The ECS Series of Texts and Monographs. Wiley, 2004.

[42] T. Y. Hou and X.-H. Wu, "A multiscale finite element method for elliptic problems in composite materials and porous media", *Journal of Computational Physics*, vol. 134, pp. 169–189, 1997.

[43] E. Weinan and B. Engquist, "The heterognous multiscale methods", *Communications in Mathematical Sciences*, vol. 1, pp. 87–132, 2003.

[44] T. J. Hughes, G. R. Feijóo, L. Mazzei, and J.-B. Quincy, "The variational multiscale method—a paradigm for computational mechanics", *Computer Methods in Applied Mechanics and Engineering*, vol. 166, pp. 3–24, 1998, Advances in Stabilized Methods in Computational Mechanics.

[45] F. Larsson, K. Runesson, and F. Su, "Variationally consistent computational homogenization of transient heat flow", *International Journal for Numerical Methods in Engineering*, vol. 81, pp. 1659–1686, 2010.

[46] F. Larsson, K. Runesson, S. Saroukhani, and R. Vafadari, "Computational homogenization based on a weak format of micro-periodicity for RVE-problems", *Computer Methods in Applied Mechanics and Engineering*, vol. 200, pp. 11–26, 2011.

[47] K. Yoo, A. Deshpande, S. Banerjee, and P. Dutta, "Electrochemical model for ionic liquid electrolytes in lithium batteries", *Electrochimica Acta*, vol. 176, pp. 301–310, 2015.

[48] J. Wesselingh, P. Vonk, and G. Kraaijeveld, "Exploring the maxwell-stefan description of ion exchange", *The Chemical Engineering Journal and the Biochemical Engineering Journal*, vol. 57, pp. 75–89, 1995.